NANO · MICRO small
www.small-journal.com

Size Selective Corona Interactions from Self-Assembled Rosette and Single-Walled Carbon Nanotubes

Xun Gong, Liang Shuai, Rachel L. Beingessner, Takeshi Yamazaki, Jianliang Shen, Matthias Kuehne, Kelvin Jones, Hicham Fenniri, and Michael S. Strano**

Nanoparticle corona phases, especially those surrounding anisotropic particles, are central to determining their catalytic, molecular recognition, and interfacial properties. It remains a longstanding challenge to chemically synthesize and control such phases at the nanoparticle surface. In this work, the supramolecular chemistry of rosette nanotubes (RNTs), well-defined hierarchically self-assembled nanostructures formed from heteroaromatic bicyclic bases, is used to create molecularly precise and continuous corona phases on single-walled carbon nanotubes (SWCNTs). These RNT–SWCNT (RS) complexes exhibit the lowest solvent-exposed surface area (147.8 ± 60 m^{-1}) measured to date due to its regular structure. Through Raman spectroscopy, molecular-scale control of the free volume is also observed between the two annular structures and the effects of confined water. SWCNT photoluminescence (PL) within the RNT is also modulated considerably as a function of their diameter and chirality, especially for the (11, 1) species, where a PL increase compared to other species can be attributed to their chiral angle and the RNT's inward facing electron densities. In summary, RNT chemistry is extended to the problem of chemically defining both the exterior and interior corona interfaces of an encapsulated particle, thereby opening the door to precision control of core–shell nanoparticle interfaces.

1. Introduction

The corona phase of a nanoparticle consists of the adsorbed molecules to its external surface.[1,2] Their formation, whether from synthesis[3,4] or the environment,[2] serves as important interfaces that control the particle's properties.[5–7] The most well-known example of corona phases occurs in the case of biomaterials,[8] where the adsorption of proteins upon exposure to a biological environment decorates the particles of interest. Subsequently, the evolution of this corona phase ultimately controls both the material fate[9,10] and eventual biological function.[11] In the case of solution synthesis of colloidal oxide nanoparticles, the establishment of surfactant corona phases serves the critical role as capping agents that assist the formation of discrete particles.[12] In addition to preventing aggregation, the adsorbed surfactant layer, in this case, can also be tuned to control both particle size and shape.[13] Similarly, corona phases are important in preventing aggregation of intrinsically hydrophobic nanomaterials in aqueous environments, including carbon nanotubes,[14,15] boron nitride nanotubes,[16] and graphene.[17]

Recently, the engineering of the single-walled carbon nanotube (SWCNT) corona phases has proven attractive for materials design due to their ability to modulate SWCNT optical and electronic properties.[18,19] Common SWCNT corona phases include surfactants, single-stranded DNA (ssDNA), proteins, and carbohydrates,[14,20] which have been engineered into constructs with applications in therapeutics, catalysis, labeling, and sensing.[21–25] Adsorbed DNA can also serve as attachment points to link multiple particles into larger structures,[26] opening the door to the design of molecular scale electronics.[27] It is important to note that these commonly employed surfactant- and polymer-based corona phases necessarily exhibit imprecise or stochastic structure. They only partially exclude the surrounding solvent[28] and rely on unstructured self-assembly. The next generation of nanostructured particles will require greater control of the molecular tolerances within assemblies. A biological cell, for example, is able to maintain electrical potentials out of equilibrium by assembling molecularly precise barriers.

X. Gong, M. Kuehne, K. Jones, M. S. Strano
Department of Chemical Engineering
Massachusetts Institute of Technology
77 Massachusetts Avenue, Building 66, Cambridge, MA 02139, USA
E-mail: strano@mit.edu
L. Shuai, R. L. Beingessner, T. Yamazaki
National Institute for Nanotechnology and Department of Chemistry
University of Alberta
11421 Saskatchewan Drive, Edmonton, Alberta T6G2M9, Canada
J. Shen
Wenzhou Institute
University of Chinese Academy of Sciences
No.16 Xinsan Road, Hi-tech Industry Park, Wenzhou
Zhejiang 325000, China
H. Fenniri
Department of Chemical Engineering
Department of Bioengineering
Department of Chemistry and Chemical Biology
Northeastern University
360 Huntington Avenue, Boston, MA 02115-5000, USA
E-mail: h.fenniri@northeastern.edu
The ORCID identification number(s) for the author(s) of this article can be found under https://doi.org/10.1002/smll.202104951.

DOI: 10.1002/smll.202104951

While regular SWCNT corona structures are hypothesized to exist, involving micellar assemblies of surfactants[29–31] or hydrogen bonding structures of DNA,[32] experimental verification is complex and often intrinsically biased. Direct imaging, including atomic force microscopy (AFM)[33] and electron microscopy,[34] invariably disturbs this fluid phase during sample preparation. Spectroscopy,[35] calorimetry,[36] and molecular adsorption studies[28] all study the corona phases through averaged or secondary effects and, thus, are unable to elucidate unique, and likely transient, surface structures existing on single particles. Two recent discoveries support the existence of regular structures within SWCNT corona phases: 1) the ability of sequence-specific DNA–SWCNT to selectively partition SWCNTs of different chiralities, with nearly identical diameters, into different solution phases,[32,37] and 2) the ability of chosen corona phases to bind specific molecules and report the event optically.[22]

To this end, an alternative strategy to SWCNT corona phase engineering is to use the tools of organic chemistry and supramolecular assembly. Previously, helical[38] and tubular[39] protein assemblies have been used to encase SWCNTs, showing chirality-dependent SWCNT dispersions. Here, we study the supramolecular assembly of rosette nanotubes (RNTs), consisting of much smaller subunits ($M_W < 700$), creating a chemically regular environment around the SWCNT. Our cursory efforts in the past suggest that such an assembly is viable.[40] RNTs are well-defined hierarchically self-assembled nanostructures with a broad range of applications in tissue engineering,[41,42] drug delivery,[43,44] and sensors.[45] The self-assembling module G0 (**Figure 1**A) investigated in this study undergoes a hierarchical self-assembly process fueled by hydrophobic effects in water to form a six-membered supermacrocycle maintained by 36 H-bonds (twin rosette). The resulting and substantially more hydrophobic twin-rosette self-organizes into a nanotube with an inner diameter (ID) of ≈11 Å, an outer diameter of ≈35 Å, and a stacking distance of ≈3.4 Å.[46–49] The observed RNT lengths range from one to tens of micrometers.[50] The inner-channel-facing functional groups of the RNT are comprised of a regular array of carbonyl and primary amine groups from the G and C bases, respectively. Upon self-assembly, any functional group covalently attached to G0 could be expressed on the surface of the nanotubes, thereby offering a general "built-in" strategy for tailoring the physical and chemical properties of the RNT.[51] Furthermore, chemical modification of the G0 module provides additional opportunity to control the inner and outer dimensions and function of the RNTs.[52–54]

In this work, we first perform the single dispersion of small-diameter semiconducting SWCNTs by the assembly of RNTs on their outside as the corona phase. Through an array of orthogonal characterization methods, we verify that RNTs form the external surface of the dispersed particles. We also show that the SWCNTs are indeed completely encapsulated within and highly isolated from the solution environment, exhibiting the lowest solvent exposed nanoparticle surface area recorded to date. Optical excitation–emission maps were taken to study the SWCNTs' first and second electronic transitions. The photoluminescence (PL) redshifts and intensity modulation give information on the differences in the SWCNT local environment inside the RNT as a function of both chirality and diameter. Taken together, this work is the first demonstration of SWCNT encapsulation within another free-standing nanotube through the process of dispersion and self-assembly. The resulting

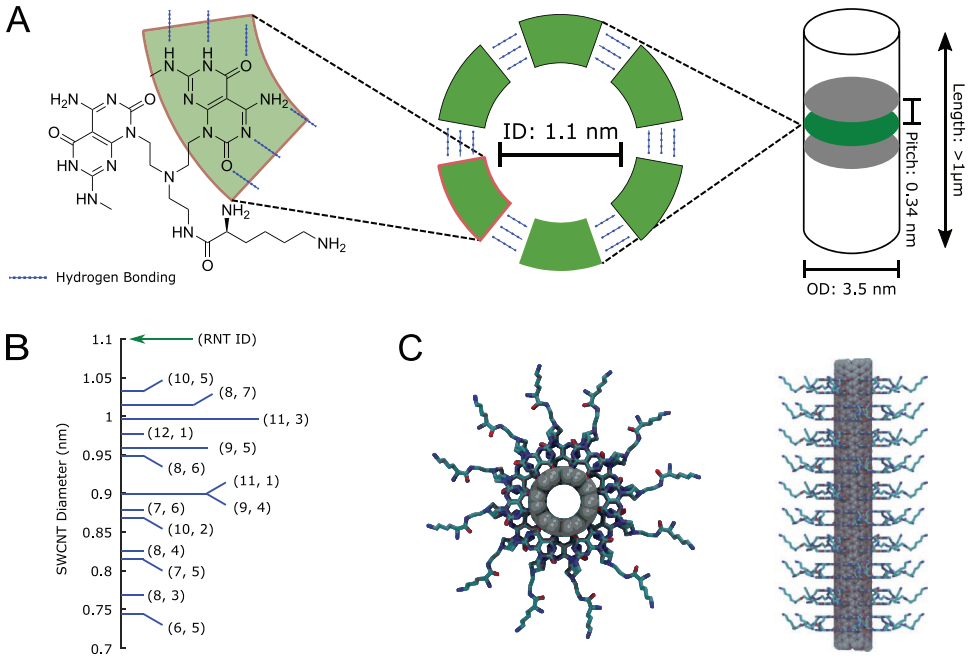

Figure 1. The dispersion of SWCNTs with RNTs as compared to other routine SWCNT wrappings. A) Structural diagram and parameters of self-assembled RNTs in aqueous solution showing the molecule structure (left), radial hydrogen bonding interactions between the molecules (middle), and the formation of the RNT longitudinally (right). B) Chart showing that the inner diameter of the RNT is larger than the diameters of the SWCNT chiralities present in a HiPco sample, making encapsulation within feasible. C) A diagram of the RS complex is shown.

RNT–SWCNT (RS) system can serve as a versatile platform that provides both a regular chemically controlled environment for the study of the SWCNT electronic structure as well as flexibility of design for the solution-facing component of the nanoparticle corona.

2. Results and Discussion

2.1. RS Dispersion and SWCNT Diameter Dependence

Small-diameter semiconducting SWCNTs made from the HiPco method (NanoIntegris) are used for this study, which usually contain a known set of SWCNT chirality species as defined by the (n, m) coordinate system.[55] Comparing the diameters of the SWCNT species present in a HiPco sample to the inner diameter of the RNT, successful encapsulation appears physically feasible (Figure 1B). Considering that the RNT inner diameter was previously calculated assuming internal water, and that the RNT hydrogen bonds are allowed for a degree of radial flexibility, the additional van der Waals radius from the encapsulated SWCNT can likely be accommodated. Figure 1C shows an SWCNT encapsulated within the RNT assembly.

Dispersion of SWCNT in aqueous solution is usually performed in two steps. First, energy input, often by tip ultrasonication, is required to separate individual SWCNTs from bundles within a solution where then the corona components can adsorb and prevent re-aggregation. Subsequently, the sample is purified through centrifugation to remove larger bundles and aggregates such that singly dispersed SWCNTs remain. For DNA corona phases, though the total amount of DNA adsorbed to SWCNT can be both sequence and chirality dependent,[56] the common convention of 1:1 weight ratio of nucleotides to SWCNT was used as a starting point since RNTs are comprised of nucleoside-like molecules. Similar to DNA–SWCNT dispersions, we expect that the van der Waals forces of these molecules allow their adsorption to the SWCNT surface, while the charged groups provide colloidal stability in the aqueous environment.

The dispersion is performed via tip ultrasonication followed by a minimum centrifugation of 60 min at 30 000 × g (additional details in the Supporting Information). We expect through this process that any existing RNT structures are first disrupted, and then re-assemble around the SWCNTs. These bundles are then removed through centrifugation prior to subsequent analysis. As a comparison, we prepared SWCNT dispersions with ssDNA $d(GT)_{15}$, sodium dodecyl sulfate (SDS), and sodium cholate (SC). The resulting dispersion yield is comparable to previous DNA–SWCNT dispersions at 189 mg L^{-1} as quantified by an extinction coefficient of 0.036 L mg^{-1} cm^{-1} at 632 nm.[28]

To study the size distribution of RNT-wrapped SWCNT, which we will refer to RS hereafter, we perform single-particle tracking (SPT) followed by the analysis using maximum a posteriori nanoparticle tracking analysis (MApNTA).[57,58] Briefly, SPT is a method of particle sizing through the observation of Brownian motion in a controlled dilute solution environment. Compared to bulk light-scattering techniques, SPT is advantageous for the study of polydispersed samples, as each particle is observed and included in the particle size distribution. We choose SPT to study new dispersions as we make no assumptions regarding monodispersity. MApNTA is a Bayesian method for estimating particle size distributions using data from SPT (additional details in the Supporting Information). The SPT results are reported as hydrodynamic radius distributions since a rigid rod assumption cannot be made (**Figure 2**A). The RNT–SWCNT dispersion shows a particle size distribution significantly larger and more polydispersed. This is expected if RNTs are indeed self-assembled properly, as they can range from 1 µm to tens of micrometers in length (Figure S2, Supporting Information).[50] There should be two major species after preparation: RNTs with SWCNTs within, and RNTs without SWCNTs within. Both species should appear to have RNT-like dimensions on the outside, larger than that of the SWCNT with surfactant or DNA corona phases, which, for the current preparation methods, range between 500 and 1500 nm in length.[58] The SC–SWCNT distribution is smaller than that of the DNA–SWCNT due to increased ultrasonication time of the method used, which decreases SWCNT length.

Absorption spectroscopy is a common tool to evaluate optical transitions of SWCNTs (Figure 2B). Comparing the E_{11} region (900–1350 nm for small-diameter SWCNTs), RS peaks are broadened and redshifted. As is common for colloidal SWCNT dispersions, these optical changes correlate with small aggregates or chemical functionalization.[59] However, in this study,

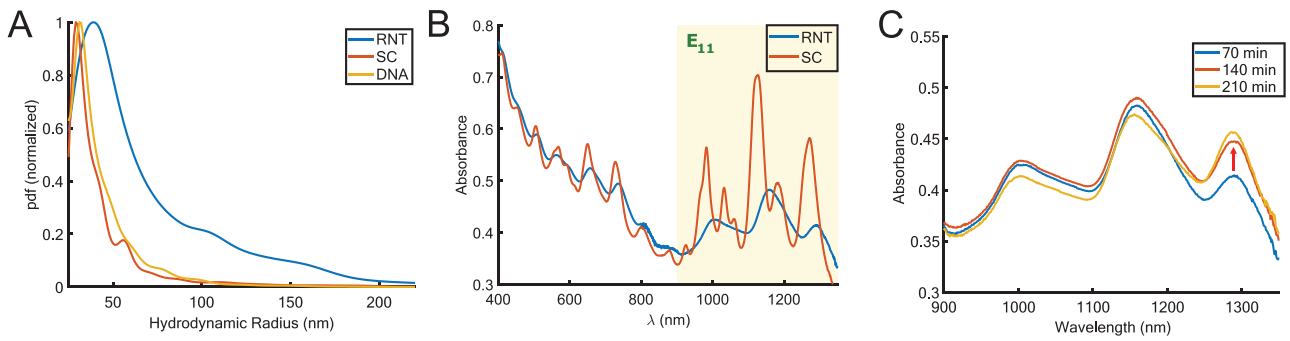

Figure 2. The dispersion quality of the RS hybrid is compared to common corona phases by two methods: A) single particle tracking for the measurement of particle size distributions and B) absorbance spectroscopy for the quantification of SWCNT and visualization of their electronic transitions. Wrapping of RNT with SWCNTs results in differences in SWCNT chirality populations post dispersion and purification. C) Zoomed-in plot of different durations of centrifugation of RS dispersion show changing chirality populations, which is shown as a relative increase of higher diameter species.

these observations are potentially attributable to the RNT encapsulation, significantly changing the SWCNT local environment.

To study whether the RNT wrapping has a chirality preference during the dispersion process, we measure absorption spectra as a function of centrifugation time. As different chirality SWCNTs are similar in buoyancy, shown in previous density gradient experiments,[60] initial centrifugation primarily serves to remove bundles and aggregates to increase the purity of singly dispersed components. Figure 2C details absorption spectral changes with increasing centrifugation with 140 min on the order of what is usually employed as a purification step for sensor applications.[23] Generally, larger-diameter SWCNTs correspond to longer-wavelength E_{11} transitions. Thus, the centrifugation step revealed a relative increase in larger-diameter SWCNTs, likely due to a preferential dispersion of certain species in the RNT system. Fitting methods[61] and prior knowledge of species present in the HiPco can be used to determine chiralities present in the sample. However, in the RS case, peak broadening, likely due to this unique corona phase, makes this process unreliable (Figure S1, Supporting Information).

2.2. The Preservation of RNT Structure around SWCNTs

To visualize the RNT encapsulation of SWCNTs, we turn to Scanning electron microscopy (SEM; **Figure 3**A). RNTs form self-assembled structures independent of the SWCNT and are known to generally survive the electron microscopy preparation process.[52] Images show tubular structures with lengths on the order of micrometers, much longer than preparations

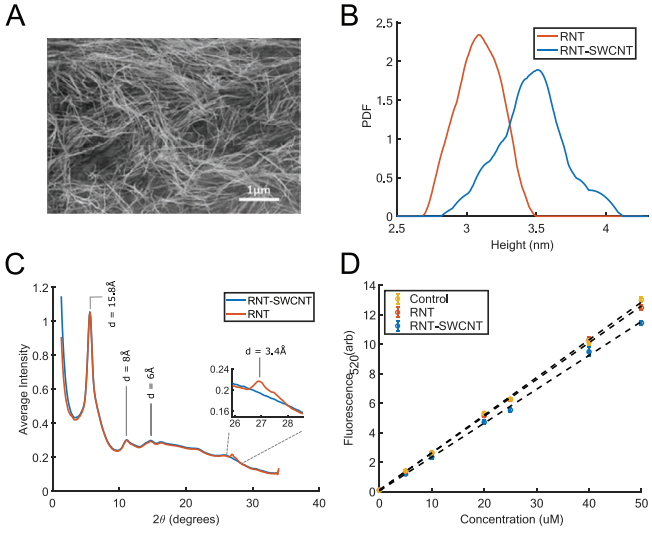

Figure 3. Study of outer RNT structure around SWCNTs. A) Electron microscopy showing that RS structures with lengths longer than the expected length of the SWCNTs within the sample. B) Quantification of AFM images of RNT versus RS show that the RNT alone is compressible, and thus a lower measured diameter. C) WAXS comparing differences between SWCNT-filled and water-filled RNTs show no significant difference, indicating that local organization in a dry sample is dominated by RNT–RNT stacking. D) The MPA method was employed with riboflavin as a probe to study the accessible surface area on the encapsulated SWCNTs, showing minimal riboflavin–SWCNT interactions in the RS sample.

of SWCNT undergone the same degree of sonication. This is the first visual evidence that the RNT is on the outside of the observed structures. AFM was performed on the RNT and RS (Figure S3, Supporting Information). The distributions of tube height show RS as consistent with the predicted RNT diameter of 35 Å, while the RNT alone measures 5 Å less (Figure 3B). This is because RNTs are soft-water-filled materials and undergo tip-induced compression in contact mode AFM.[62,63] The lack of compression in the case of SC is another indication that SWCNTs are indeed encapsulated within the RNTs.

When dried, RNT is also known to retain predictable packing as shown from a previous X-ray diffraction study.[49] Here we perform wide-angle X-ray scattering (WAXS) on samples with or without encapsulated SWCNT (Figure 3C). Characteristic peaks from RNT bundling are observed in both experimental and control conditions. Consistent with previous work,[64] the bundles formed 2D hexagonal packing with characteristic peaks ($2\theta = 6.1$, 14, and 21). SWCNT bundles are unlikely to be present due to our separation by centrifugation. The absence of major differences between WAXS results indicates that RNT–RNT interactions dominate in a dried sample, which supports the observation that the SWCNTs are encapsulated within. There is also a disruption of the rosette regular z-stacking in the RS sample (inset: $d = 3.4$ Å). This is likely from the misalignment of the internal regular SWCNT electron density with that of the RNT assembly, which forces the noncovalent structure of the RNT to adapt.

As the RNT is a densely packed structure, the SWCNT within can be thought of being highly isolated from the solution environment. This can be tested using a method we developed, called molecular probe adsorption (MPA).[28] In MPA, a small fluorescent molecule that quenches upon interaction with the nanomaterial surface is chosen as a molecular probe. This way, probing the accessible areas through the corona can be quantified through fluorescence observations. Riboflavin is chosen due to its $\pi--\pi$ stacking affinities for nanocarbons such as SWCNTs.

In our MPA study, the probe can exist in three states: free, bound to SWCNT, or bound to the outer RNT. Assuming a type-1 Langmuir isotherm and performing the appropriate adsorption site balance, we arrive at

$$C_{Rb} + q_{RNT} C_{RNT} \frac{C_{Rb}}{C_{Rb} + K_{D,RNT}} + q C_{RS} \frac{C_{Rb}}{C_{Rb} + K_D} = C_{total} \quad (1)$$

where C_{Rb}, C_{RNT}, and C_{RS} are concentrations of riboflavin, RNT, and RS, respectively. q is the surface coverage, and K_D is the dissociation constant of the riboflavin to the accessible sites on the nanoparticle surface. Thus, we can use $\frac{q}{K_D}$ as a normalized quantity to numerically compare the amount of SWCNT surface exposed to an external probe. The smaller the quantity, the larger the proportion of nanoparticle surface that is covered by the corona phase. Calculation of this value requires the collection of riboflavin fluorescence titrations as control, then in the presence of RNT, and finally in the presence of RS (Figure 3D). The RNT-associated adsorption values can be fitted first, which then leaves a single $\frac{q}{K_D}$ quantity for binding to the SWCNT surface to fit using the RS titration (additional methods in the Supporting Information).

The riboflavin titration shows minimum adsorption to the RNT alone, and an increased amount of adsorption to RS, showing that there are SWCNT surfaces exposed. The calculated surface coverage value for RS is $\frac{q}{K_D} = 147.8 \pm 60\,\text{M}^{-1}$. Literature values for common corona phases that are used to create stable aqueous SWCNT solutions are ssDNA $(GTTT)_7$ [438.5 m^{-1}], ssDNA $(GT)_{15}$ [503.7 m^{-1}], SDS [991.8 m^{-1}], and dextran [1825 m^{-1}].[28] "In comparison, the RS corona phase surface coverage of the SWCNT is the highest observed to date." The MPA study is functional evidence of the preservation of the tightly packed RNT structure after the formation of the RS complex. It is important to note that surface coverage should not be expected to be 100% as every SWCNT sample inevitably contains a distribution of defects, kinks, and endcaps.

2.3. Photophysical Study of Local SWCNT Dielectric Environment within the RNT

To study the effects of RNT encapsulation on the SWCNT optical properties, we employ excitation–emission mapping. For a mixture of singly dispersed multichirality small-diameter semiconducting SWCNT sample, we excite with visible light (E_{22} = 500–850 nm) and record NIR PL emissions (E_{11} = 900–1400 nm). In the excitation–emission map, each major peak corresponds to a specific chirality of SWCNT based on their first and second electronic transitions (**Figure 4**A,B). Converting wavelength to energy, and SWCNT chirality to diameter, the information extracted can be displayed through a Kataura plot (Figure 4C).[65] Comparison with the Kataura plots for SC and SDS SWCNT dispersions (Figure S4, Supporting Information) makes it apparent that both E_{11} and E_{22} of RS are redshifted by up to 6 meV compared to SWCNTs suspended in vacuum. This result is congruent with the observation of redshifts in the absorption spectroscopy data from Figure 2.

In addition to emission energy shifts, interactions between the SWCNT and the local environment can also modulate PL intensity. In the case of RS, the PL signal is decreased overall compared to that of the SC, requiring a sixfold increase in integration time to achieve a comparable signal. Excitation–emissions maps for SC, SDS, and chitosan dispersions of SWCNT are displayed in Figure S5 (Supporting Information) for comparison. To study the chirality-dependent effect of the RNT on SWCNT PL emission intensity, we perform a corona phase exchange on RS with sodium dodecylbenzene sulfonate (SDBS) to recover any quenching effects. The exchange was performed by diluting RS into 2% SDBS and then bath sonicating 1 h to insure completion. The exchange resulted in a PL intensity distribution similar to that of the other surfactant dispersions (Figure S5, Supporting Information), with an increased preference for large-diameter species. To quantitate the effects of the RNT on SWCNT PL, we normalize to that of the SDBS exchanged sample. Each sample is first normalized to its (6, 5) intensity, the usually highest PL chirality. Then ratios of the RS PL values for each chirality to their SDBS exchanged counterparts were taken and presented as a plot of SWCNT diameter and chiral angle (Figure 4D). Two significant observations can be made: 1) PL increase correlates with SWCNT diameter, and

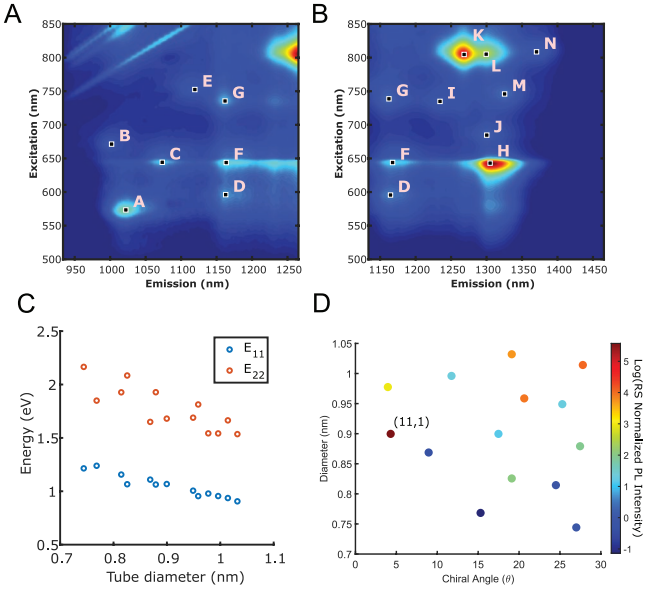

Figure 4. Differences between RNT wrapping of different SWCNT chiralities can be studied via SWCNT electronic transitions. A,B) Fluorescence microscopy constructed SWCNT excitation–emission maps. SWCNT species are labeled—A: (6, 5), B: (8, 3), C: (7, 5), D: (8, 4), E: (10, 2), F: (7, 6), G: (9, 4), H: (11, 1), I: (8, 6), J: (9, 5), K: (12, 1), L: (11,3), M: (8, 7), and N: (10,5). C) Kataura plot showing the electronic transitions of semiconducting SWCNTS extracted from excitation–emission map. D) The log of the PL intensity of RS is normalized to that of RS exchanged with SDBS and plotted on an SWCNT diameter versus chiral angle axis, showing a diameter dependence on PL as well as the unique response of the (11, 1) species.

2) a preferential PL increase for the (11, 1) chirality of 263 times was observed. Of note, this minor SWCNT chirality within the HiPco sample is often not observed.

To first explain the observed wavelength shift of the electronic transitions, we first introduce an interaction between the exciton and the local environment through an effect called solvatochromism. Solvatochromism was first studied in organic fluorophores but since then has been extended to nanomaterials.[66,67] When an exciton is created in an SWCNT from optical absorption, the excited state interacts with the surrounding environment before relaxing to the ground state. Due to the timescale of fluorescence emission, the solvent molecules have a chance to rotationally reorient to stabilize with respect to the dipole of the exciton. The energy cost results in an increase in the emission wavelength, which is observed as a redshift. It is important to note that this can occur with any surrounding molecule, not just solvents.

The SWCNT can be modeled as a series of isolated molecular fluorophores with the number of solvent interactions per length as a function of the SWCNT radius. Intuitively, the amount of solvatochromic shift should scale inversely with SWCNT radius due to the increase of solvent interactions per carbon atom from tube curvature. This relationship can be modeled as a comparison to observations made in air.[68] Empirically based on several independent data sets, Choi and Strano found that solvatochromic shift of singly isolated SWCNT consistently followed the linear relationship[69]

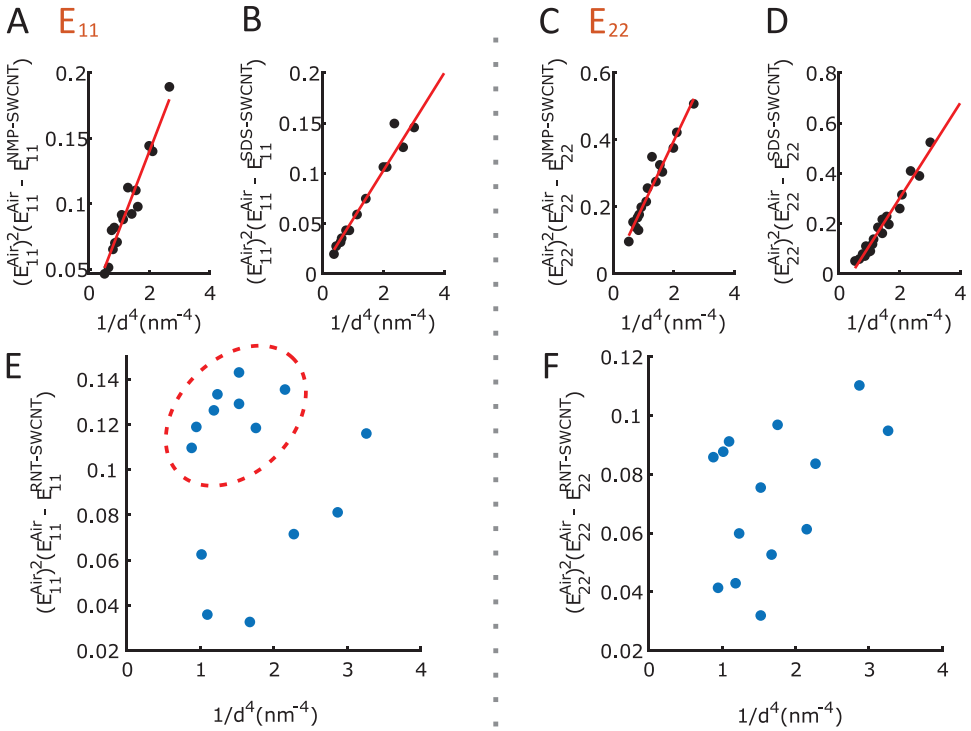

Figure 5. ΔE versus $1/d^4$ plots, a linear solvatochromic shifts model, is used to compare different SWCNT dispersions with RS. Reference A,C) *N*-methyl-2-pyrrolidone (NMP) and B,D) sodium dodecyl sulfate (SDS) data[69] are shown for E,F) E_{11} (left) and E_{22} (right) transitions to compare with that of the RS. RS showed decreased linearity in both cases, especially for E_{11} where a select group of SWCNT chiralities (circled) deviated significantly from the prior linear model.

$$(E_{ii})^2 \Delta E_{ii} = \frac{c}{R^4} \tag{2}$$

where E_{ii} is the electronic transition measured in air, and ΔE_{ii} is the electronic transition in air minus that of the experiment. c is an aggregate proportionality constant that describes solvent or local environment properties. R is the radius of the SWCNT. Using this equation, we plot $(E_{ii})^2\Delta E_{ii}$ versus $\frac{1}{R^4}$ for the RNT-wrapped samples for both E_{11} and E_{22} (**Figure 5**A,B). *N*-methyl-2-pyrrolidone (NMP) and SDS data were reproduced from Choi and Strano as a comparison.[69] While the linear correlation coefficients in the NMP and SDS cases were greater than 0.95, they were 0.02 and 0.44 for RS at E_{11} and E_{22}, respectively. Specifically, the solvatochromic shift for E_{11} of RS increased for a group of chiralities as the SWCNT diameter approached 1 nm. This indicates that there is a significant change in the local environment as a function of increasing SWCNT diameter. A similar effect is observed in the E_{22} of RS, albeit to a lesser extent.

The explanation of the SWCNT diameter dependence can be found with Raman spectroscopy. Specifically, we examine the radial breathing mode (RBM) of the RS SWCNT. Briefly, Raman spectroscopy is a vibrational spectroscopy based on inelastic light scattering that is commonly employed to study carbon nanomaterials.[70] In the specific case of SWCNTs, a characteristic peak at 200–300 cm^{-1} can be observed corresponding to all C atoms vibrating in the radial direction with the same phase. Using elastic theory, the RBM location can be modeled as a function of SWCNT diameter

$$\omega_{RBM} = \frac{A}{d_t} + B; A = \sqrt{Y/\rho} \tag{3}$$

where d_t is the SWCNT diameter, Y is the Young's modulus, and ρ is the density. B is a positive fitting constant that takes into account environmental influences and is theoretically zero for an isolated SWCNT in vacuum. Examples of these environmental effects include the surrounding medium, adsorbed molecules, and bundling. The existence of B or a redshift can be thought of as the additional energy required to displace the surrounding medium during the radial movement. For example, the RBM peaks are sensitive to SWCNT wrapping, with the worse wrapped cases (more water exposure) resulting in a larger B value or redshift.[71]

Figure 6A depicts the RBM region of the Raman spectra for RNT and SDS wrapped SWCNT. Comparing the five observable peak locations, the RNT sample shows relative shifts in both directions. Due to the number of species and uniqueness of the RNT construct, a deconvolution was not performed. To estimate SWCNT diameter correlating to the observed peaks from the SC data, we use $A = 218.3$ cm^{-1} nm and $B = 15.9$ cm^{-1} measured from a HiPco sample in literature.[72] Plotting the difference between RBM of the two samples versus SWCNT diameter, we observe three distinct regions (Figure 6B). When the SWCNT diameter is small, RBM_{RNT} is greater than RBM_{SC},

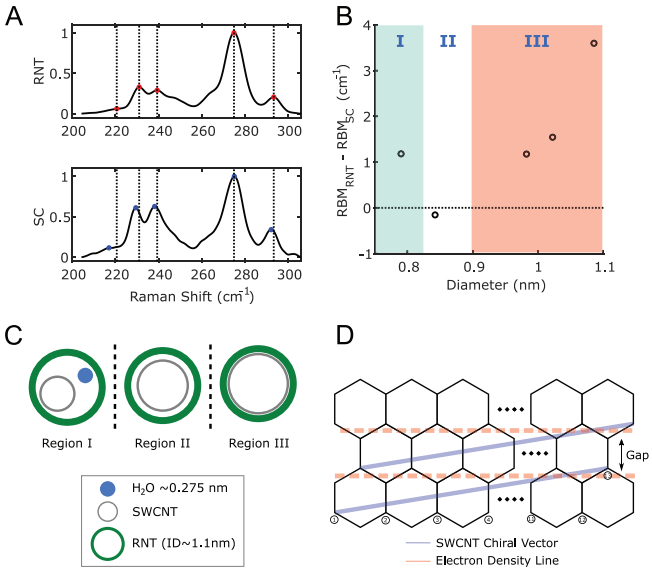

Figure 6. A) RBM regions of the RS and SC–SWCNT Raman spectra is plotted. B) Differences in RBM peak Raman shifts are plotted versus diameter. Different regions of the proposed SWCNT local environment are labeled (green: solvent, white: solvent excluded, and red: increasing RNT). C) Schematic of the three cases proposed, where region I—SWCNT is encapsulated with water, region II—water is excluded in between, and region III—SWCNT diameter approaches RNT ID. D) "Unrolled" diagram of electron density for a (11, 1) SWCNT, showing minimal crossing of electron densities per revolution.

appearing as if the SWCNT is poorly wrapped with high-solvent exposure (green: region I). As the SWCNT diameter increases, encapsulated water is excluded, leaving space between itself and the RNT structure. Compared to the surfactant sample, this case may have less molecular adsorption, and thus is slightly blueshifted (white: region II). Finally, as the SWCNT approaches the RNT inner diameter, increasing interactions with the RNT result in incremental redshift as a function of the SWCNT diameter (red: region III), an observation we also made in Figure 4D.

To explain the three-region observation, we compare the geometry of the species involved (Figure 6C). RNT without SWCNT can be thought of as filled with water molecules during the assembly process. For small-diameter SWCNTs, they can coexist with water molecules within the RNT, thus emulating the solvatochromic shift consistent with water exposure. Knowing that the inner diameter of the RNT is ≈11 Å and that of a water molecule is ≈2.75 Å, as the SWCNT diameter increases past ≈8 Å, water molecules are excluded. However, due to the polar inward-facing groups of the RNT, solvatochromic effects increase as the SWCNT increases further. Thus, there exists a blueshifted SWCNT PL region where the water is excluded and the RNT is maximally away.

The diameter-dependent PL change from Figure 4D can also be explained through the exclusion of water. As for the significant relative PL increases of the (11, 1) chirality, we consider the structure of the RNT together with SWCNT molecular structure (Figure 6D). The RNT can be thought of as a set of regularly spaced monomers, each contributing two functional groups inward with regular radial spacing and stacking pitch.[53] Since the pitches of the two tubes are unequal due to geometric constraints of the SWCNT, the RNT noncovalent stacking regularity is disrupted to accommodate, as shown by the WAXS data. This interaction also affects the excitons on the SWCNT surface.

The SWCNT structure can be approximated as a set of electron density lines (Figure 6D). The angle of the chiral vector determines the number of times these lines are crossed per revolution of the tube. For any SWCNT with $m < 1$, there exists a maximally spaced region between the electron density lines at one C—C bond apart. This allows the RNT electron densities to offset most optimally in the longitudinal direction. Coincidentally, (11, 1) SWCNT contains 12 electron densities radially, which also allows for the offset of the 12 radial contributions of the RNT, 2 from each of the G^C base. Metallic SWCNTs with zero m coordinate cannot be observed with a PL study due to the lack of bandgap florescence.

3. Conclusion

In this work, we demonstrated the colloidal encapsulation of SWCNTs by self-assembled RNTs. Through imaging, X-ray scattering, and spectroscopy, we orthogonally verified that SWCNTs can be indeed singly wrapped within the RNT structure with the RNTs form the outer component of a large population of the dispersed particles. Using fluorescent riboflavin as adsorption probes to query the accessible surface area on the SWCNT, we find little riboflavin quenching from interactions with the SWCNT surface. Comparing to other common SWCNT dispersions measured to date, we conclude that the RNT forms the most tightly packed corona phase around an SWCNT in aqueous solution, enabling improved control over solution phase interactions.

The dispersion process also shows that the RNTs selectively wrap larger-diameter SWCNT species in a HiPco sample. A similar diameter-dependent trend was observed when looking at SWCNT PL intensity. By interrogating the population of singly dispersed SWCNTs within the RNTs, we observe a selective PL signal increase for the (11, 1) SWCNT species. This can be explained by comparing SWCNT electron density with that of the RNT interior, where the chiral angle of the (11, 1) species allowed for optimal electron density offset.

Finally, we study the SWCNT local environment within the RNT via Raman spectroscopy. Observed Raman RBM shifts show that the SWCNT experiences three distinct local environment regimes from 0.7 to 1.1 nm within the RNT, a region where the SWCNT co-exists with encapsulated water, another where water is excluded, and a third where the SWCNT approaches the RNT inner diameter. The water exclusion from the encapsulation significantly reduces solvatochromic effects, explaining the diameter dependence of the observed photoluminesence.

The dispersion of SWCNTs from aggregates is one of the first steps toward unlocking some of its unique material properties. Choosing the appropriate corona phase is an important design step toward its various applications. The encapsulation of SWCNTs within a regularly self-assembled structure provides a unique toolkit for the custom design of corona phases with unprecedented control. More importantly, these constructs

enable the study of SWCNT photophysics given a molecularly regular environment.

4. Experimental Section

Materials: All chemicals were purchased from Sigma–Aldrich (USA) unless stated otherwise. ssDNA sequences were purchased from Integrated DNA Technologies (IDT, USA). HiPCO SWCNTs were used for all experiments and were purchased from (Nanointegris, Boisbriand, Quebec, Canada).

Rosette Material Synthesis: Module G0 was synthesized and purified according to the previously reported procedure.[73]

Preparation of SWCNT Dispersions: SWCNT dispersions were prepared by combining 1 mg of SWCNTs and 1 mg of RNT in 1 mL in deionized (DI) water. This mixture was tip-sonicated (Qsonica Q125) in an ice bath with a 0.125 in. probe for 30 min at a power of 4 W. Crude SWCNT dispersions were centrifuged at 30 100 × *g* for 70 min intervals (number of times as specified) to remove SWCNT bundles and other solid impurities. The top 80% of supernatant was collected after each round of centrifugation.

Absorbance, Photoluminescence, and Raman Spectroscopy: Absorbance spectra of SWCNT dispersions were collected (Cary 5000, Agilent Technologies) to approximate the concentrations of the postdispersion stock solutions using the absorbance at 632 nm and an extinction coefficient of ε_{632} = 0.036 (mg $L^{-1})^{-1}$ cm^{-1}. Photoluminescence was performed on a customized NIR microscope, which consists of a Zeiss Axio Vision inverted Microscope body with a 20× objective, coupled to an Acton SP2500 spectrometer and a liquid-nitrogen-cooled InGaAs 1D detector (Princeton Instruments). Excitation–emission maps were constructed by tracking the fluorescence spectrum from 950 to 1250 nm while stepping the excitation from 500 to 800 nm in 5 nm increments. A 1 W broadband white laser (NKT Photonics) was coupled to a tunable filter with a 2 nm bandwidth (Photon Etc.). Wavelength calibration was performed using an argon lamp and the NIST spectra line database. Intensity correction was performed using power measured at sample location for each wavelength of excitation, as specified by the tunable filter, using a microscope slide power sensor. Peak shape was partly cut off due to grating switch, but did not affect peak center interpretation. Raman spectroscopy was performed using a Horiba LabRAM HR with a 532 nm laser through a 100 × objective (Olympus MplanFL N, Numerical Aperture = 0.9). The sample was drop-casted on a glass slide and integrated spatially.

Single-Particle Tracking: SPT studies were performed on a NanoSight LM10 (Malvern, USA). NanoSight software, NTA3.1, was used for video analysis to yield tracks. MATLAB implementation of above equations was used for subsequent calculations and plotting. A Harvard Apparatus (Holliston, MA) Pump 11 Elite syringe pump was used to advance samples at 50 µL min^{-1} over 6 s to advance particle frame. Sample preparation involved dilution within the appropriate solvent until ≈200 particles were observed. For data analysis of particle tracks, MApNTA implemented in MATLAB was utilized.[54,55]

Sample Preparation for Electron Microscopy: Modules G0 (1 mg mL^{-1}) were dissolved in unbuffered dH_2O (deionized water) at 90 °C and allowed to age for 2 days at room temperature (final pH = 5.5).

TEM and SEM Imaging: Transmission electron microscopy (TEM) samples were prepared by floating a carbon-coated 400 mesh copper grid on a droplet of G0 (1 mg mL^{-1} in dH_2O) for 25 s. The samples were stained by floating the grid consecutively on two droplets of 1% aqueous uranyl acetate for 20 s each. The grid was then blotted, dried in air, and viewed in a JEOL 2010 microscope operating at 200 kV.

SEM images of the RNTs on carbon-coated 400 mesh copper grid were recorded on a Hitachi S-4800 operating at 5 kV. Uranyl-acetate-stained samples were prepared as described above. Unstained samples were prepared by placing a carbon-coated 400 mesh copper grid on a 1 mg mL^{-1} droplet of three solutions for 25 s. The grids were then blotted and dried in air before imaging.

AFM Imaging: Silicon substrates (1 × 1 cm^2) were cleaned in a 3:1 sulfuric acid:30% hydrogen peroxide solution (piranha solution) for 15 min. The substrates were then thoroughly rinsed with dH_2O. The native SiO_x layer was converted to SiH_x by placing the substrates in 48% hydrofluoric acid solution for 5 min. AFM measurements were performed in tapping mode (TM-AFM) at a scan rate of 2 Hz per line using a Digital Instruments/Veeco Instruments MultiMode Nanoscope IV equipped with an E scanner. Silicon cantilevers (MikroMasch USA, Inc.) were used with spring constants of 40 N m^{-1}. The RNT samples were prepared by spin-coating 30 µL of a 1 mg mL^{-1} solution on a Si/SiH_x at 2000 rpm for 30 s. Note that TM-AFM tends to compress soft materials and result in lower height profiles. Since the rigid core of the RNTs was 3.0 nm in diameter, the expected lower limit of the height profile by AFM in tapping mode should be close to this number.[63]

X-Ray Scattering: The WAXS system uses a Rigaku 002 microfocus X-ray source with osmic-staggered parabolic multilayer optics to focus the beam. The X-ray source was operated at full power which was 45 kV and 0.66 mA. The programs used to remotely control the system were Ganesha System Control and Ganesha Interactive Control Center (GICC). The 4 mm diameter samples were deposited, dried, and sandwiched between two pieces of Kapton tape and placed on the Ambient 8 × 8 Holder. In addition to the two samples tested, a reference sample of silver behenate was measured. Measurements were performed below 0.08 mbar. The silver behenate reference sample was measured at 60 s exposure. For the two samples of interest, the exposure was set to 600 s.

MPA Surface Area: The free surface area of the polymer-wrapped SWNT was estimated using a molecular probe adsorption technique. Fluorescence calibration curves of riboflavin from 0 to 5 × 10^{-6} m were measured using a Thermo VarioSkan Plate Reader. Riboflavin was excited at 460 nm, and emission was collected from 510 to 540 nm. Deflections of the riboflavin fluorescence were taken in the presence of 10 mg mL^{-1} RNT, and a solution of 10 mg L^{-1} SWCNT dispersed with RNT. The surface area was estimated according to Park et al.[28]

Data Processing: All data processing, fitting, and statistical analysis were performed in MATLAB (Natik, MA).

Supporting Information

Supporting Information is available from the Wiley Online Library or from the author.

Acknowledgements

Experiments were performed by X.G. Preliminary encapsulation experiments, imaging modeling, and data analysis were carried out by L.S., R.L.B., T.Y., and J.S. The manuscript was written by X.G., H.F., and M.S.S. All authors have approved the final version of the manuscript. The authors thank K. S. Silmore for performing part of the supplemental SEM imaging.

Conflict of Interest

The authors declare no conflict of interest.

Data Availability Statement

The data that support the findings of this study are available from the corresponding author upon reasonable request.

Keywords

nanomaterial dispersion, rosette nanotubes, self-assembly, single-walled carbon nanotubes

Received: August 17, 2021
Revised: November 24, 2021
Published online: January 21, 2022

[1] M. P. Monopoli, C. Aberg, A. Salvati, K. A. Dawson, *Nat. Nanotechnol.* **2012**, *7*, 779.
[2] P. Rivera-Gil, D. Jimenez De Aberasturi, V. Wulf, B. Pelaz, P. Del Pino, Y. Zhao, J. M. De La Fuente, I. Ruiz De Larramendi, T. Rojo, X.-J. Liang, W. J. Parak, *Acc. Chem. Res.* **2013**, *46*, 743.
[3] K. Reed, A. Cormack, A. Kulkarni, M. Mayton, D. Sayle, F. Klaessig, B. Stadler, *Environ. Sci.: Nano* **2014**, *1*, 390.
[4] C. Walkey, S. Das, S. Seal, J. Erlichman, K. Heckman, L. Ghibelli, E. Traversa, J. F. McGinnis, W. T. Self, *Environ. Sci.: Nano* **2015**, *2*, 33.
[5] C. A. S. Batista, R. G. Larson, N. A. Kotov, *Science* **2015**, *350*, 1242477-1.
[6] S. F. Oliveira, G. Bisker, N. A. Bakh, S. L. Gibbs, M. P. Landry, M. S. Strano, *Carbon* **2015**, *95*, 767.
[7] Y. Hoshino, H. Lee, Y. Miura, *Polym. J.* **2014**, *46*, 537.
[8] O. Vilanova, J. J. Mittag, P. M. Kelly, S. Milani, K. A. Dawson, J. O. Rädler, G. Franzese, *ACS Nano* **2016**, *10*, 10842.
[9] M. Hadjidemetriou, K. Kostarelos, *Nat. Nanotechnol.* **2017**, *12*, 288.
[10] S. Bhattacharya, D. Roxbury, X. Gong, D. Mukhopadhyay, A. Jagota, *Nano Lett.* **2012**, *12*, 1826.
[11] S. Khan, A. Gupta, C. K. Nandi, *J. Phys. Chem. Lett.* **2013**, *4*, 3747.
[12] T.-D. Nguyen, *Nanoscale* **2013**, *5*, 9455.
[13] Y. Yin, A. P. Alivisatos, *Nature* **2005**, *437*, 664.
[14] R. Haggenmueller, S. S. Rahatekar, J. A. Fagan, J. Chun, M. L. Becker, R. R. Naik, T. Krauss, L. Carlson, J. F. Kadla, P. C. Trulove, D. F. Fox, H. C. DeLong, Z. Fang, S. O. Kelley, J. W. Gilman, *Langmuir* **2008**, *24*, 5070.
[15] V. A. Sinani, M. K. Gheith, A. A. Yaroslavov, A. A. Rakhnyanskaya, K. Sun, A. A. Mamedov, J. P. Wicksted, N. A. Kotov, *J. Am. Chem. Soc.* **2005**, *127*, 3463.
[16] Z. Gao, C. Zhi, Y. Bando, D. Golberg, T. Serizawa, *ACS Appl. Mater. Interfaces* **2011**, *3*, 627.
[17] M. Lotya, P. J. King, U. Khan, S. De, J. N. Coleman, *ACS Nano* **2010**, *4*, 3155.
[18] M. J. O'Connell, S. M. Bachilo, C. B. Huffman, V. C. Moore, M. S. Strano, E. H. Haroz, K. L. Rialon, P. J. Boul, W. H. Noon, C. Kittrell, J. Ma, R. H. Hauge, R. B. Weisman, R. E. Smalley, *Science* **2002**, *297*, 593.
[19] V. Schroeder, S. Savagatrup, M. He, S. Lin, T. M. Swager, *Chem. Rev.* **2019**, *119*, 599.
[20] V. Zorbas, A. L. Smith, H. Xie, A. Ortiz-Acevedo, A. B. Dalton, G. R. Dieckmann, R. K. Draper, R. H. Baughman, I. H. Musselman, *J. Am. Chem. Soc.* **2005**, *127*, 12323.
[21] A. Al Faraj, *Nanomedicine* **2016**, *11*, 1431.
[22] J. Zhang, M. P. Landry, P. W. Barone, J.-H. Kim, S. Lin, Z. W. Ulissi, D. Lin, B. Mu, A. A. Boghossian, A. J. Hilmer, A. Rwei, A. C. Hinckley, S. Kruss, M. A. Shandell, N. Nair, S. Blake, F. Şen, S. Şen, R. G. Croy, D. Li, K. Yum, J.-H. Ahn, H. Jin, D. A. Heller, J. M. Essigmann, D. Blankschtein, M. S. Strano, *Nat. Nanotechnol.* **2013**, *8*, 959.
[23] D. P. Salem, X. Gong, A. T. Liu, K. Akombi, M. S. Strano, *Anal. Chem.* **2020**, *92*, 916.
[24] Z. W. Ulissi, F. Sen, X. Gong, S. Sen, N. Iverson, A. A. Boghossian, L. C. Godoy, G. N. Wogan, D. Mukhopadhyay, M. S. Strano, *Nano Lett.* **2014**, *14*, 4887.
[25] M. Hu, Z. Yao, X. Wang, *Ind. Eng. Chem. Res.* **2017**, *56*, 3477.
[26] E. Penzo, M. Palma, R. Wang, H. Cai, M. Zheng, S. J. Wind, *Nano Lett.* **2015**, *15*, 6547.
[27] M. Zhao, Y. Chen, K. Wang, Z. Zhang, J. K. Streit, J. A. Fagan, J. Tang, M. Zheng, C. Yang, Z. Zhu, W. Sun, *Science* **2020**, *368*, 878.
[28] M. Park, D. P. Salem, D. Parviz, X. Gong, K. S. Silmore, T. T. S. Lew, D. T. Khong, M. C.-Y. Ang, S.-Y. Kwak, M. B. Chan-Park, M. S. Strano, *Nano Lett.* **2019**, *19*, 7712.
[29] A. Striolo, B. P. Grady, *Langmuir* **2017**, *33*, 8099.
[30] C. Richard, F. Balavoine, P. Schultz, T. W. Ebbesen, C. Mioskowski, *Science* **2003**, *300*, 775.
[31] Q. Wang, Y. Han, Y. Wang, Y. Qin, Z.-X. Guo, *J. Phys. Chem. B* **2008**, *112*, 7227.
[32] X. Tu, S. Manohar, A. Jagota, M. Zheng, *Nature* **2009**, *460*, 250.
[33] P. V. Jena, Y. Shamay, J. Shah, D. Roxbury, N. Paknejad, D. A. Heller, *Carbon* **2016**, *97*, 99.
[34] X. Gong, A. K. Sharma, M. S. Strano, D. Mukhopadhyay, *ACS Nano* **2014**, *8*, 9126.
[35] M. P. Landry, S. Kruss, J. T. Nelson, G. Bisker, N. M. Iverson, N. F. Reuel, M. S. Strano, *Sensors* **2014**, *14*, 16196.
[36] G. Bisker, N. A. Bakh, M. A. Lee, J. Ahn, M. Park, E. B. O'Connell, N. M. Iverson, M. S. Strano, *ACS Sens.* **2018**, *3*, 367.
[37] J. A. Fagan, *Nanoscale Adv.* **2019**, *1*, 3307.
[38] G. Grigoryan, Y. H. Kim, R. Acharya, K. Axelrod, R. M. Jain, L. Willis, M. Drndic, J. M. Kikkawa, W. F. DeGrado, *Science* **2011**, *332*, 1071.
[39] F. A. Mann, J. Horlebein, N. F. Meyer, D. Meyer, F. Thomas, S. Kruss, *Chemistry* **2018**, *24*, 12241.
[40] J.-Y. Cho, T. Yamazaki, J. G. Duque, S. Doorn, S. Das, M. Green, H. Fenniri, *TechConnect Briefs* **2013**, *1*, 31.
[41] X. Zhou, S. Tenaglio, T. Esworthy, S. Y. Hann, H. Cui, T. J. Webster, H. Fenniri, L. G. Zhang, *ACS Appl. Mater. Interfaces* **2020**, *12*, 33219.
[42] X. Zhou, T. Esworthy, S.-J. Lee, S. Miao, H. Cui, M. Plesiniak, H. Fenniri, T. Webster, R. D. Rao, L. G. Zhang, *Nanomedicine* **2019**, *19*, 58.
[43] J.-Y. Cho, P. Bhowmik, P. L. Polowick, S. G. Dodard, M. El-Bakkari, G. Nowak, H. Fenniri, U. D. Hemraz, *ACS Omega* **2020**, *5*, 24422.
[44] Y. Fan, A. C. Pauer, A. A. Gonzales, H. Fenniri, *Int. J. Nanomed.* **2019**, *14*, 7281.
[45] P. Tripathi, L. Shuai, H. Joshi, H. Yamazaki, W. H. Fowle, A. Aksimentiev, H. Fenniri, M. Wanunu, *J. Am. Chem. Soc.* **2020**, *142*, 1680.
[46] H. Fenniri, P. Mathivanan, K. L. Vidale, D. M. Sherman, K. Hallenga, K. V. Wood, J. G. Stowell, *J. Am. Chem. Soc.* **2001**, *123*, 3854.
[47] R. S. Johnson, T. Yamazaki, A. Kovalenko, H. Fenniri, *J. Am. Chem. Soc.* **2007**, *129*, 5735.
[48] T. Yamazaki, H. Fenniri, A. Kovalenko, *ChemPhysChem* **2010**, *11*, 361.
[49] H. Fenniri, G. A. Tikhomirov, D. H. Brouwer, S. Bouatra, M. El Bakkari, Z. Yan, J.-Y. Cho, T. Yamazaki, *J. Am. Chem. Soc.* **2016**, *138*, 6115.
[50] J. Raez, J. G. Moralez, H. Fenniri, *J. Am. Chem. Soc.* **2004**, *126*, 16298.
[51] G. Tikhomirov, M. Oderinde, D. Makeiff, A. Mansouri, W. Lu, F. Heirtzler, D. Y. Kwok, H. Fenniri, *J. Org. Chem.* **2008**, *73*, 4248.
[52] G. Borzsonyi, R. L. Beingessner, T. Yamazaki, J.-Y. Cho, A. J. Myles, M. Malac, R. Egerton, M. Kawasaki, K. Ishizuka, A. Kovalenko, H. Fenniri, *J. Am. Chem. Soc.* **2010**, *132*, 15136.
[53] H. Fenniri, B.-L. Deng, A. E. Ribbe, K. Hallenga, J. Jacob, P. Thiyagarajan, *Proc. Natl. Acad. Sci. USA* **2002**, *99*, 6487.
[54] R. Chhabra, J. G. Moralez, J. Raez, T. Yamazaki, J.-Y. Cho, A. J. Myles, A. Kovalenko, H. Fenniri, *J. Am. Chem. Soc.* **2010**, *132*, 32.
[55] I. W. Chiang, B. E. Brinson, A. Y. Huang, P. A. Willis, M. J. Bronikowski, J. L. Margrave, R. E. Smalley, R. H. Hauge, *J. Phys. Chem. B* **2001**, *105*, 8297.
[56] R. Nißler, F. A. Mann, P. Chaturvedi, J. Horlebein, D. Meyer, L. Vuković, S. Kruss, *J. Phys. Chem. C* **2019**, *123*, 4837.

[57] K. S. Silmore, X. Gong, M. S. Strano, J. W. Swan, *ACS Nano* **2019**, *13*, 3940.
[58] X. Gong, M. Park, D. Parviz, K. S. Silmore, P. Gordiichuk, T. T. S. Lew, M. S. Strano, *Small* **2019**, *15*, 1901468.
[59] A. V. Naumov, S. Ghosh, D. A. Tsyboulski, S. M. Bachilo, R. B. Weisman, *ACS Nano* **2011**, *5*, 1639.
[60] F. Bonaccorso, T. Hasan, P. H. Tan, C. Sciascia, G. Privitera, G. Di Marco, P. G. Gucciardi, A. C. Ferrari, *J. Phys. Chem. C* **2010**, *114*, 17267.
[61] M. Pfohl, D. D. Tune, A. Graf, J. Zaumseil, R. Krupke, B. S. Flavel, *ACS Omega* **2017**, *2*, 1163.
[62] A. L. Slade, C. M. Yip, in *Molecular Interfacial Phenomena of Polymers and Biopolymers* (Ed: P. Chen), Woodhead Publishing, Duxford, UK **2005**, pp. 161–213.
[63] M. Knez, M. P. Sumser, A. M. Bittner, C. Wege, H. Jeske, D. M. P. Hoffmann, K. Kuhnke, K. Kern, *Langmuir* **2004**, *20*, 441.
[64] M. C. García-Gutiérrez, A. Nogales, J. J. Hernandez, D. Rueda, T. Ezquerra, *Opt. Pura Apl.* **2007**, *40*, 195.
[65] H. Kataura, Y. Kumazawa, Y. Maniwa, I. Umezu, S. Suzuki, Y. Ohtsuka, Y. Achiba, *Synth. Met.* **1999**, *103*, 2555.
[66] P. Suppan, *J. Photochem. Photobiol., A* **1990**, *50*, 293.
[67] S. Nigam, S. Rutan, *Appl. Spectrosc.* **2001**, *55*, 362A.
[68] S. M. Bachilo, M. S. Strano, C. Kittrell, R. H. Hauge, R. E. Smalley, R. B. Weisman, *Science* **2002**, *298*, 2361.
[69] J. H. Choi, M. S. Strano, *Appl. Phys. Lett.* **2007**, *90*, 223114.
[70] A. Jorio, R. Saito, G. Dresselhaus, M. S. Dresselhaus, in *Raman Spectroscopy in Graphene Related Systems*, John Wiley & Sons, Ltd, Hoboken, NJ **2011**, pp. 199–222.
[71] Q.-H. Yang, N. Gale, C. J. Oton, F. Li, A. Vaughan, R. Saito, I. S. Nandhakumar, Z.-Y. Tang, H.-M. Cheng, T. Brown, W. H. Loh, *Nanotechnology* **2007**, *18*, 405706.
[72] L. G. Moura, M. V. O. Moutinho, P. Venezuela, F. Mauri, A. Righi, M. S. Strano, C. Fantini, M. A. Pimenta, *Carbon* **2017**, *117*, 41.
[73] J. G. Moralez, J. Raez, T. Yamazaki, M. R. Kishan, A. Kovalenko, H. Fenniri, *J. Am. Chem. Soc.* **2005**, *127*, 8307.

